Journal of Materials Chemistry C

PAPER

View Article Online
View Journal | View Issue

Cite this: J. Mater. Chem. C, 2017, 5, 2282

Building block magneto-luminescent nanomaterials of iron-oxide/ZnS@LaF_3:Ce^{3+},Gd^{3+},Tb^{3+} with green emission†

Navadeep Shrivastava,[ab] L. U. Khan,[b] Z. U. Khan,[c] J. M. Vargas,[d] O. Moscoso-Londoño,[e] Carlos Ospina,[f] H. F. Brito,[b] Yasir Javed,[g] M. C. F. C. Felinto,[h] A. S. Menezes,[a] Marcelo Knobel[ef] and S. K. Sharma*[a]

The preparation of novel triply-doped bifunctional Fe_3O_4/ZnS@LaF_3:$x$$Ce^{3+}$,$x$$Gd^{3+}$,$y$$Tb^{3+}$ (x = 5; y = 5, 10 and 15 mol%) nanocomposites with efficient optical and magnetic features has been reported. The ZnS semiconductor functionalized Fe_3O_4 particles were coated with LaF_3:RE^{3+} materials *via* a chitosan-assisted co-precipitation method. The size of iron oxide ~7.2 nm and trigonal structures of bifunctional nanostructures were confirmed through X-ray diffraction and high-resolution transmission electron microscopy. The static magnetic measurements supported and manifested the superparamagnetic behavior of the materials at 300 K. A broad emission band was observed in the blue region (400–550 nm) due to the sulphur vacancy on the surface of the Fe_3O_4/ZnS nanocomposite. For a triply doped bifunctional nanostructure, the excitation spectra revealed broad absorption bands centered at around 270 nm, which were attributed to the 4f($^7F_{7/2}$) → 5d interconfigurational transition of the Ce^{3+} ion accompanied by narrow absorption lines arising from the 4f–4f intraconfigurational transitions of the Tb^{3+} ion. The emission spectra of the nanocomposites showed characteristic narrow emission lines assigned to the $^5D_4$ → ^7F_J transitions (J = 6–0) of the Tb^{3+} ion. The energy transfer process from the Ce^{3+} → Gd^{3+} → Tb^{3+} ions has also been presented and discussed. Furthermore, the structural, photoluminescence and magnetic properties of Fe_3O_4/ZnS@LaF_3:RE^{3+} suggested that it may be an efficient candidate for magnetic light-converting molecular devices (MLMCDs) and high energy radiation detection.

Received 21st November 2016,
Accepted 25th January 2017

DOI: 10.1039/c6tc05053k

rsc.li/materials-c

1 Introduction

During the last decade, the design and engineering of bifunctional nanosized materials by co-assembling magnetic and photonic features into a single entity nanostructure have gained remarkable attention due to their promising applications in optoelectronics and scintillation of ionizing radiations.[1–5] These nanomaterials are also widely used as multifunctional biomarkers in various biomedical applications such as *in vitro* and *in vivo* labeling,[6,7] quantitative DNA analyses,[8] bioimaging,[9] and magnetic hyperthermia for cancer therapy.[10,11] Therefore, various approaches have been reported to design efficient multifunctional nanomaterials. Usually, the preparation methods of these bifunctional nanostructures include coating or layer-by-layer deposition of rare earth (RE) phosphors or quantum dots on magnetic core nanoparticles[12–14] and polymer-assisted encapsulation of magnetic nanoparticles with luminophores in single nanostructures.[15] Functionalization of Fe_3O_4 with fluorescent dyes or luminescent d-transition metal complexes is another method for the synthesis of bifunctional nanomaterials.[2,16,17]

Among the iron oxide nanostructures, magnetite exhibits long-range ordering of magnetic moment, high surface-to-volume ratio and low toxicity as compared to its parent bulk counterpart. However, the bare Fe_3O_4 nanoparticles are highly vulnerable to self-aggregation and an air atmosphere causes their partial oxidation to maghemite (γ-Fe_2O_3).[18,19] Usually, iron oxide is a strong

[a] Department of Physics, Federal University of Maranhão, Av. dos Portugueses, 1966 – Bacanga, São Luís – MA, 65080-805, Brazil. E-mail: surender76@gmail.com
[b] Department of Fundamental Chemistry, Institute of Chemistry, University of São Paulo, Av. Prof. Lineu Prestes, 748, 05508-000, São Paulo-SP, Brazil
[c] Department of Immunology, Institute of Biomedical Sciences-IV, University of São Paulo, Av. Prof. Lineu Prestes, 1730, 05508-000, São Paulo-SP, Brazil
[d] Consejo Nacional de Investigaciones Científicas y Técnicas (CONICET), Centro Atómico Bariloche, Av. Bustillo 9500, 8400, San Carlos de Bariloche, Río Negro, Argentina
[e] Institute of Physics "GlebWataghin", State University of Campinas (UNICAMP), 13083-859, Campinas-SP, Brazil
[f] Brazilian Nanotechnology National Laboratory (LNNano–CNPEM), Rua Giuseppe Máximo Scolfaro 10000, 13083-100, Campinas-SP, Brazil
[g] Department of Physics University of Agriculture, Faisalabad, Pakistan
[h] Nuclear and Energy Research Institute – IPEN, University of São Paulo, Av. Prof. Lineu Prestes, 2242, 05508-000, São Paulo-SP, Brazil

† Electronic supplementary information (ESI) available: HR-TEM, EDS, PL, and M–H at 5 K and ZFC/FC. See DOI: 10.1039/c6tc05053k

luminescence quencher. This phenomenon occurs *via* an energy transfer process; when a luminescent center (*e.g.*, RE^{3+} ion) comes into contact directly or in proximity with the magnetic metal oxide surface (Fe_3O_4).[15,20] In order to overcome this drawback, the intermediate layers, spacers or energy barriers are usually introduced in between the iron oxide nanoparticles and luminophores. Therefore, iron oxide nanoparticles can be coated with organic macrocycles, polymers, silica or semiconductors before introducing the luminophores to prepare such bifunctional nanomaterials. It helps to retain their magnetic and luminescence features in the same nanoentity. The magnetic properties of these bifunctional nanomaterials originate directly from the iron oxide NPs in combination with the magnetic moments of the RE^{3+} ions.

Zinc sulfide (ZnS) is an important semiconductor and a classical scintillating material with remarkable physical and chemical properties. The great advantages of the ZnS material are: large energy band gap (3.72 eV), considerable excitonic binding energy (40 meV), fluorescence property, environmentally-friendly nature, relatively low price and simple synthesis procedure.[21] Therefore, ZnS is a suitable luminophore to synthesize highly-photostable fluorescent and magnetic Fe_3O_4/ZnS nanomaterials.[21–23] Besides, this nanocomposite structure may act as an energy barrier or a separator between the Fe_3O_4 magnetic nanoparticles and RE^{3+} luminophores to lower luminescence quenching phenomena although being a composite material. In this system, Fe_3O_4 acts as a semi-metal with a small band gap and can be expected to quench the luminescence of the ZnS due to the leakage path provided by magnetite to excited electrons.[24] This may protect the direct contact of magnetite with rare earth luminophores and lower the quenching due to the interaction between iron oxide and LaF_3:RE^{3+} luminophores. The Fe_3O_4/ZnS nanocomposite does not affect the magnetic characteristics so much. Thus the magneto-luminescence characteristics of the Fe_3O_4/ZnS nanocomposite can be manipulated under an external magnetic field.

The luminescent RE^{3+} nanomaterials present remarkable optical characteristics by exhibiting narrow emission bands from the visible to near infrared range with relatively long lifetimes and high quantum yields.[25–27] The photoluminescence properties of the RE^{3+} ions originate mainly due to the 4f energy-level structures, which are negligibly affected by the chemical environment due to the effective shielding of the 4f electrons by the externally filled 5s and 5p sub-shells.[25,28,29] Therefore, the absorption and emission spectra of the 4f intraconfigurational transitions of the RE^{3+} ions retain more or less their atomic character and show narrow absorption and emission bands.[2,30] The optical energy transfer mechanism depends strongly on the selection of a host lattice. For example, LaF_3 is considered as an ideal diamagnetic host matrix for the exploitation of electronic transitions and the magnetic contribution of dopant RE^{3+} ions,[31] the reason being the size compatibility with the other trivalent rare earth ions following the Vegard law. This rule establishes a limit of around 15% of the size of RE^{3+} to obtain complete solid solubility between the dopant and the host ion.[28,32,33] The LaF_3 matrix allows a high ionic character of the RE^{3+} and the F^- bond leading to a wide band gap, low vibration energies ($<350\ cm^{-1}$), minimal quenching of the electron–hole (e–h) and better chemical stability. These properties make it a versatile host matrix.[4,28,34] The very low vibration energy of the host matrix is an important factor as it protects the dopant ions from deactivation sources through nonradiative decays. This leads towards high emission quantum efficiency. The dopant RE^{3+} ions are selectively chosen to achieve efficient intramolecular energy transfer from sensitizers to the activator ions. These are primary criteria to obtain a highly luminescent nanomaterial.

One of the most intense emitting RE^{3+} ions is Tb^{3+} with many distinct advantages.[35,36] It is paramagnetic at room temperature,[37] ultrasensitive (*in vivo* and *in vitro*), highly luminescent and monochromatic. The narrow emission bands of Tb^{3+} ion arising from 4f–4f transitions are independent of the chemical environment. On the other hand, the Ce^{3+} ion presents f–d interconfigurational transition (4f–5d) and can be used as a sensitizer in combination with the Tb^{3+} activator, since it provides an easy indirect energy transfer pathway from Ce^{3+} to Tb^{3+} ions.[36,38] There are few reports that show the use of the Ce^{3+} ion as a sensitizer in X-ray luminescence and also its potential application in high-energy radiation detection even in an aqueous medium, where it is soluble.[38,39] The coexistence of the paramagnetic Gd^{3+} ($4f^7$) with Tb^{3+} and Ce^{3+} ions, having a large energy gap ($32\,000\ cm^{-1}$) between the $^8S_{7/2}$ and first-excited $^6P_{7/2}$ energy level, supports the efficient energy transfer mechanism from Ce^{3+} to Tb^{3+} ions in the LaF_3 host matrix in a cascaded way. The Gd^{3+} ion has another unique characteristic. It is sensitive to neutron flux in the radiation detection mechanism with the highest stable neutron cross section.[38,40]

In this work, the preparation, structural and morphological characterization as well as photoluminescence and magnetic properties of the (i) Fe_3O_4/ZnS and (ii) bifunctional inorganic Fe_3O_4/ZnS@LaF_3:$x$$Ce^{3+}$,$x$$Gd^{3+}$,$y$$Tb^{3+}$ (x = 5; y = 5, 10 and 15 mol%) nanomaterials have been reported. The DC magnetic properties (M–H and ZFC/FC curves) were studied in order to analyze the magnetic information over the final structure of the bifunctional nanocomposite. Moreover, the photoluminescence properties based on the excitation/emission spectral data and luminescence decay curves are also investigated and discussed in detail. The Fe_3O_4/ZnS together with the RE^{3+} ion doped LaF_3 luminescent materials makes the multistep synthesized nanocomposite applicable in downshift processes *e.g.*, in high energy radiation detection as well as in magnetic light-converting molecular devices.

2 Experimental section

2.1. Synthesis

The commercially available chemical reagents were used without further purification. $FeCl_2{\cdot}4H_2O$, $NH_3{\cdot}H_2O$ and oleic acid were purchased from Synth and $Zn(O_2CCH_3)_2(H_2O)_2$ from Alfa Aesar. NaOH, NH_4F, hydrochloric acid and nitric acid were obtained from VETEC. Thioacetamide was purchased from Merck and cetyltrimethylammonium bromide (CTAB) from Sigma-Aldrich. $LaCl_3{\cdot}6H_2O$, $GdCl_3{\cdot}6H_2O$, $TbCl_3{\cdot}6H_2O$ and

$Ce(NO_3)_3{\cdot}6H_2O$ were synthesized from their respective oxide sources *i.e.* La_2O_3, Gd_2O_3, Tb_4O_7 and CeO_2 (99.99%) obtained from Rodhia.

Fe_3O_4 nanoparticles. The hydrothermal method was used to prepare oleic acid coated magnetic core nanoparticles, according to previous reports published elsewhere.[12,41] 3.0 g (75 mmol) of NaOH and 30.0 g (95.4 mmol) of oleic acid (90 wt%) were mixed in 40.0 mL of ethanol and stirred at room temperature till the formation of a white viscous solution. Furthermore, a dark brown color suspension appeared immediately after pouring 60 mL of an aqueous solution of $FeCl_2{\cdot}4H_2O$ (0.1 mol L^{-1}) into the above solution. This solution was vigorously stirred for 30 minutes and a brown precipitate was formed. Then, the reaction mixture was transferred into a 150 mL autoclave. It was sealed and heated at 180 °C for 10 h. After that the system was allowed to cool to room temperature. The product was collected at the bottom of the vessel and washed first with *n*-butanol and then with water and ethanol. The washed material was dried under reduced pressure in a vacuum desiccator.

Fe_3O_4/ZnS nanoparticles. In a typical procedure,[42] 0.3 g (1.29 mmol) of as-prepared Fe_3O_4 particles were dispersed in 100 mL *n*-propanol by adding a solution of 0.44 g (2.0 mmol) of $Zn(O_2CCH_3)_2(H_2O)_2$ in 60 mL *n*-propanol. This reaction mixture was stirred at room temperature for 24 h. Thereafter, 60 mL of 0.2 g (2.66 mmol) thioacetamide in Milli-Q water was added dropwise to the above solution. Simultaneously, the resulting solution was heated at 65 °C under vigorous stirring for 5 h. Then, the reaction mixture was cooled to room temperature and gently stirred overnight. The solid product was collected by a magnetic separation method and washed five times with water and ethanol to remove the excess ZnS nanoparticles. Finally, it was dried under reduced pressure for 12 h and stored in a vacuum desiccator.

Fe_3O_4/ZnS@LaF_3:$x$$Ce^{3+}$,$x$$Gd^{3+}$,$y$$Tb^{3+}$ nanocomposites. The optical and magnetic Fe_3O_4/ZnS@LaF_3:$x$$Ce^{3+}$,$x$$Gd^{3+}$,$y$$Tb^{3+}$ (x = 5; y = 5, 10 and 15 mol%) nanomaterials were prepared by the chitosan-assisted coprecipitation method through a general procedure using a specific amount of Fe_3O_4/ZnS nanoparticles and stoichiometric amounts of $LaCl_3{\cdot}6H_2O$, $Ce(NO_3)_3{\cdot}6H_2O$, $GdCl_3{\cdot}6H_2O$ and $TbCl_3{\cdot}6H_2O$ precursors.[43] In this procedure, 0.1 g of Fe_3O_4/ZnS nanoparticles was dispersed in 20 mL of Milli-Q water through ultrasonication. Furthermore, a 4 mL (0.1 mol L^{-1}) aqueous solution of cetyltrimethylammonium bromide (CTAB) was added to the above mixture and stirred for 1 h to obtain an Fe_3O_4/ZnS@CTAB dispersion (solution A). Thereafter, 0.4876 g (1.3792 mmol) $LaCl_3{\cdot}6H_2O$, 0.0302 g (0.0812 mmol) $GdCl_3{\cdot}6H_2O$, 0.0352 g (0.0812 mmol) $Ce(NO_3)_3{\cdot}6H_2O$ and 0.0303 g (0.0812 mmol) $TbCl_3{\cdot}6H_2O$ were dissolved together in a 25 mL solution of 0.2 g chitosan in acetic acid/Milli-Q water (5 v/v%) in a three-necked round-bottomed flask under magnetic stirring. The pH of the solution was adjusted to 7 by dropwise addition of $NH_3{\cdot}H_2O$ (28% v/v) (solution B). 20 mL of aqueous dispersion of Fe_3O_4/ZnS@CTAB (solution A) was directly added to solution B and stirred under a continuous N_2 atmosphere. 15 mL of aqueous NH_4F solution [0.1802 g; 4.86 mmol] was injected slowly to the reaction mixture. Finally, it was heated under refluxing conditions for 3 h under continuous N_2 flow. The brown color suspension was cooled to room temperature, and the solid sample was separated from the aqueous suspension using magnetic separation. The collected solid material was washed with Milli-Q water and methanol. The brown Fe_3O_4/ZnS@LaF_3:$x$$Ce^{3+}$,$x$$Gd^{3+}$,$y$$Tb^{3+}$ (x = y = 5 mol%) was dried in a vacuum desiccator and heated in an oven at 80 °C. The other two bifunctional nanomaterials with RE^{3+} concentrations of x = 5; y = 10 and 15 mol% were also prepared by the same procedure by changing the stoichiometric values. The products were found to be water dispersible.

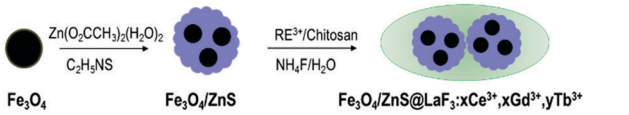

Fig. 1 Synthesis scheme for the Fe_3O_4/ZnS@LaF_3:$x$$Ce^{3+}$,$x$$Gd^{3+}$,$y$$Tb^{3+}$ (x = 5; y = 5, 10 and 15 mol%) bifunctional green-emitting magnetic nanocomposite.

The general synthesis route for the green-emitting magnetic Fe_3O_4/ZnS@LaF_3:$x$$Ce^{3+}$,$x$$Gd^{3+}$,$y$$Tb^{3+}$ nanocomposite is presented in Fig. 1.

2.2. Characterization

The phase structures of the nanocomposites were evaluated on Bruker's D8 Advance diffractometer operating with Cu $K_{\alpha 1}$ radiation at a wavelength of 0.15405 nm in the range of $10^\circ \leq 2\theta \leq 90^\circ$ (angle). The samples were analyzed by Transmission Electron Microscopy (TEM) and Energy-Dispersive X-ray Spectroscopy (EDS) using the JEM-2100F and the Titan Cubed Themis 300 microscopes, respectively, of the Electron Microscopy Laboratory (LME) at the Brazilian Nanotechnology National Laboratory (LNNano). The samples were prepared by dispersing the dry powders of the Fe_3O_4 nanoparticles in toluene, Fe_3O_4/ZnS in isopropyl alcohol and the Fe_3O_4/ZnS@LaF_3:RE^{3+} nanocomposite in distilled water through 15 min of ultrasonication. The dispersion of each sample was deposited dropwise on the 400 mesh copper grids with an ultrathin carbon film of lacey carbon and dried in an open atmosphere. High-resolution TEM images, scan mode images and EDS techniques were applied in this analysis.

The excitation and emission spectra of the Fe_3O_4/ZnS and Fe_3O_4/ZnS@LaF_3:$x$$Ce^{3+}$,$x$$Gd^{3+}$,$y$$Tb^{3+}$ nanomaterials were recorded using a SPEX FL212 Fluorolog-2 spectrofluorometer using a 450 W Xenon lamp as an excitation source and two 0.22 m double-grating SPEX 1680 monochromators for dispersing the radiation. Luminescence decay curves of the Tb^{3+} doped nanomaterials were measured using the SPEX 1934D phosphorimeter accessories attached to the 150 W pulsed xenon lamps. All spectra were recorded for the dried powder samples and automatically corrected for the instrumental and photomultiplier (PMT) response. The entire luminescence setup was fully controlled using a DM3000F spectroscopic computer program.

DC magnetic studies were carried out using a MPMS XL Quantum Design SQUID magnetometer with a field range of ±2 T and at a temperature from 5 K to 300 K. The magnetic properties of all the samples were evaluated by the hysteresis

loop (magnetization as a function of the applied field) at 5 and 300 K as well as Zero Field Cooling/Field Cooling (ZFC/FC) measurements. For ZFC/FC measurements, the sample was first cooled down from 300 K to 5 K in a zero magnetic field, then a static magnetic field of 50 Oe was applied and the magnetization was measured increasing the temperature up to room temperature (300 K). Subsequently, the sample was cooled down to 5 K under the same applied magnetic field (50 Oe), and the magnetization was measured while warming up the samples from 5 K to 300 K.

3 Results and discussion

3.1. Morphological and structural analyses

Powder x-ray diffraction (PXRD) patterns of Fe_3O_4, Fe_3O_4/ZnS and Fe_3O_4/ZnS@LaF_3:$x$$Ce^{3+}$,$x$$Gd^{3+}$,$y$$Tb^{3+}$ (x = 5; y = 5, 10 and 15 mol%) nanocomposites have been presented in Fig. 2. The average crystallite size was found to be 7.2 nm for Fe_3O_4 NPs showing the cubic structure of magnetite (iron(II/III) oxide, Fe_3O_4), corresponding to the reported reference pattern (ICDD PDF No. 19-0629).[39] The PXRD pattern (Fig. 2b) of the Fe_3O_4/ZnS nanocomposite was matched with the reference pattern ICDD PDF No. 12-0688 of the wurtzite ZnS hexagonal structure along with the minor peaks of Fe_3O_4 revealing the composite structure. All the diffraction patterns of Fe_3O_4/ZnS@LaF_3:$x$$Ce^{3+}$,$x$$Gd^{3+}$,$y$$Tb^{3+}$ nanocomposites with concentration x = 5; y = 5, 10 and 15 mol% have been shown in Fig. 2c–e respectively. These diffraction peaks were indexed and matched with the reference pattern ICDD PDF No. 32-0483.

It suggested a trigonal structure (space group $P\bar{3}c1$, group number 165) for LaF_3 with small shifting, *vis-à-vis* the existence of peaks of Fe_3O_4 and Fe_3O_4/ZnS nanosystems. The relative intensities of the PXRD peaks of LaF_3:$x$$Ce^{3+}$,$x$$Gd^{3+}$,$y$$Tb^{3+}$ were found to be much stronger and dominant in comparison to those of the Fe_3O_4 and Fe_3O_4/ZnS nanostructures. Furthermore, it was observed that an increase in the molar concentration of Tb^{3+} ion in the LaF_3 matrix resulted in a minor change in the profile of the diffraction peaks.

The high-resolution TEM (HR-TEM) image of the iron oxide NPs showed a majority of small particles (Fig. 3a, left) with their size between 6 nm and 8 nm of a spherical faceted shape. The inverse spinel structure of Fe_3O_4 has been confirmed from the fast Fourier transform (FFT) analysis, indexed along the [211] zone axis (ZA) (Fig. 3a, right).

Furthermore, the existence of aggregated particles with an average size of 30 nm was observed for the Fe_3O_4/ZnS material (Fig. 3b, left). These particles showed spherical faceted polyhedral shapes and mass–thickness contrast. The Fe_3O_4/ZnS samples presented a mixture of the Fe_3O_4 cubic and the ZnS hexagonal structures showing *d*-spacings of (100) and (002) planes of the ZnS (highlighted in red) and the (113) plane of the inverse spinel Fe_3O_4 structure, in yellow (Fig. 3b right), corroborating through the PXRD pattern. The microstructure of Fe_3O_4/ZnS@LaF_3:$x$$Ce^{3+}$,$x$$Gd^{3+}$,$y$$Tb^{3+}$ (x and y = 5 mol%) nanoparticles was studied by HR-TEM (Fig. 3c, left), showing the presence of Fe_3O_4 (cubic), ZnS (hexagonal) and LaF_3 (trigonal structure).

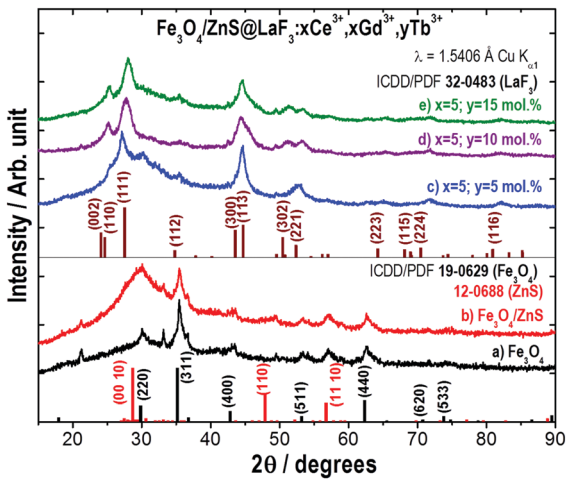

Fig. 2 PXRD patterns of Fe_3O_4 (a), Fe_3O_4/ZnS (b), Fe_3O_4/ZnS@LaF_3:$x$$Ce^{3+}$, $x$$Gd^{3+}$,$y$$Tb^{3+}$ (x = 5; y = 5, 10, 15 mol%) (c–e).

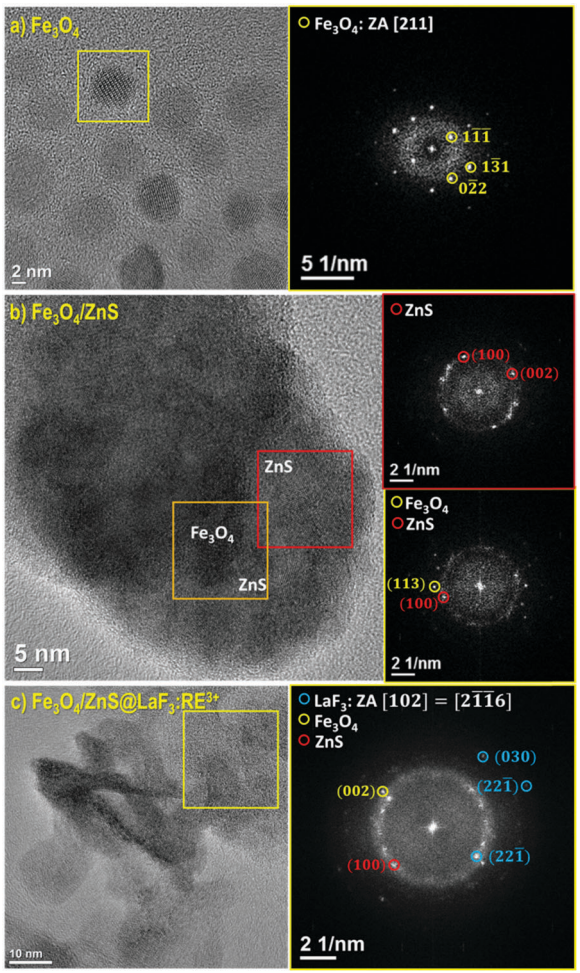

Fig. 3 HR-TEM images of inverse spinel Fe_3O_4 (a), hexagonal Fe_3O_4/ZnS (b), trigonal Fe_3O_4/ZnS@LaF_3:$x$$Ce^{3+}$,$x$$Gd^{3+}$,$y$$Tb^{3+}$ (x and y = 5 mol%) (c) samples, obtained using the JEM-2100F microscope. The regions of the images analyzed using fast Fourier transform (FFT) are highlighted.

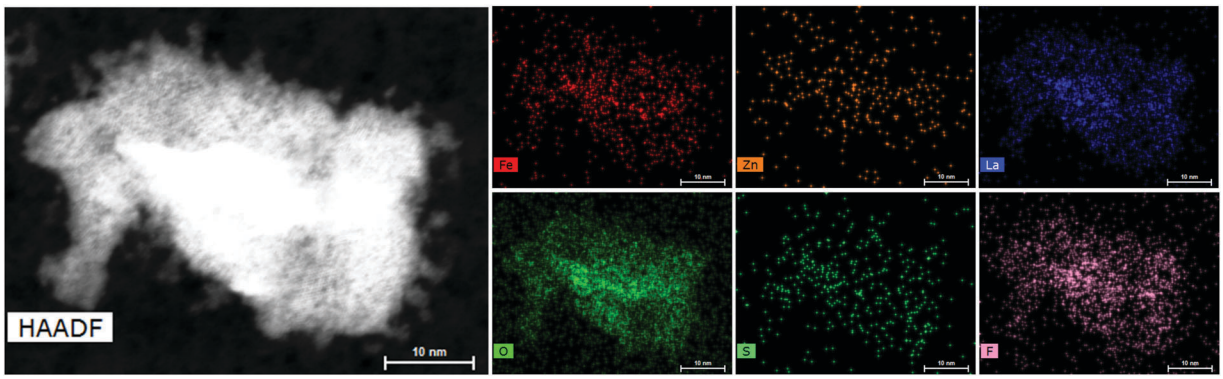

Fig. 4 High-angle annular dark-field (HAADF) image and EDS elemental mappings of the Fe_3O_4/ZnS@LaF_3:xCe^{3+},xGd^{3+},yTb^{3+} (x = y = 5 mol%) nanocomposite obtained using the Titan Cubed Themis 300 microscope, showing the homogeneous and uniform distribution of Fe, O, Zn, S, La, and F elements.

The Fast Fourier Transform (FFT) analysis showed the LaF_3 structure near the [102] = [2−1−16] zone axis, as well as the presence of the (002) and (100) planes, which corresponds to Fe_3O_4 and ZnS structures, respectively (Fig. 3c, right). The crystalline properties of all bifunctional nanocomposites indicated dimer-like particles and are closer to the polycrystalline-like structure.

High-angle annular dark-field (HAADF) and energy dispersive X-ray spectroscopy (EDS) analyses for elemental mapping (Fig. 4 and Fig. S1 of ESI†) illustrate the homogeneous distributions of Fe, O, Zn, S, La, and F along with rare earth dopants. The average % elemental composition analysis of lanthanides obtained by EDS spectra (Fig. S1C, ESI†) of Fe_3O_4/ZnS@LaF_3:xCe^{3+},xGd^{3+},yTb^{3+} (x and y = 5 mol%) shows La (79.1 ± 2.1%), Ce (7.6 ± 1.1%), Gd (6.2 ± 1.3%) and Tb (7.2 ± 2.2%).

Additional HR-TEM images, EDS mapping and EDS spectra of Fe_3O_4/ZnS@LaF_3:xCe^{3+},xGd^{3+},yTb^{3+} (x and y = 5 mol%) nanocomposites have been provided in the ESI.†

3.2. Photoluminescence properties

Fe_3O_4/ZnS luminescence. The excitation spectrum (Fig. 5a) of the Fe_3O_4/ZnS nanoparticles was recorded in the range from 200 nm to 400 nm at 300 K, monitoring the emission at 440 nm. It displayed a weak intensity broad absorption band centered at around 316 nm, which could be assigned to the band edge transition of ZnS. The band gap of the ZnS semiconductor usually occurs in the range of 3.93–4.01 eV, which corresponds to the wavelength spectral range from 315 nm to 309 nm.[44] On the other hand, the emission spectrum of the Fe_3O_4/ZnS nanomaterial was recorded at 300 K, in the range 350–700 nm upon excitation at around 316 nm assigned to the band edge transition of the ZnS (Fig. 5b). This emission spectrum revealed a low intensity broad emission band centered at around 440 nm. This blue emission broadband usually originates due to the surface defect states such as sulfur vacancies located at the surface of ZnS nanoparticles.[45]

The optical data suggested the functionalization of Fe_3O_4 with ZnS and corroborated with the observed X-ray diffraction and HR-TEM analyses.

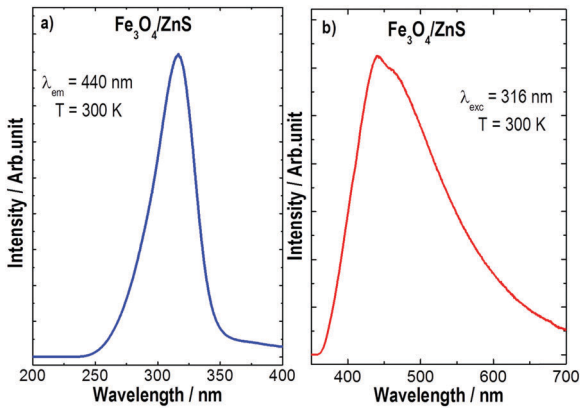

Fig. 5 Luminescence spectra of the Fe_3O_4/ZnS nanoparticles recorded at room temperature (300 K): (a) excitation spectrum, monitoring emission at 440 nm and (b) emission spectrum upon excitation at 316 nm which corresponds to the band edge transition of ZnS (3.9 eV).

Fe_3O_4/ZnS@LaF_3:xCe^{3+},xGd^{3+},yTb^{3+} green phosphors. The excitation spectra of the Fe_3O_4/ZnS@LaF_3:xCe^{3+},xGd^{3+},yTb^{3+} (x = 5; y = 5, 10 and 15 mol%) nanophosphors were recorded from 240 nm to 470 nm at 300 K (Fig. 6a), monitoring the emission at 543 nm, assigned to the higher intensity $^5D_4 \rightarrow {}^7F_5$ transition of the Tb^{3+} ion. The excitation spectra of all nanomaterials presented a high intensity broad absorption band centered at around 258 nm, corresponding to the 4f($^2F_{5/2}$) → 5d interconfigurational transition of the Ce^{3+} ion. Besides, the nanocomposite materials showed narrow absorption lines, assigned to the 4f^8–4f^8 transitions of the Tb^{3+} ion such as: $^7F_6 \rightarrow {}^5L_{8,7,6}$ and $^5G_2$ (339 nm), $^7F_6 \rightarrow {}^5L_9$ and $^5G_4$ (351 nm), $^7F_6 \rightarrow {}^5L_{10}$ (369 nm) and $^7F_6 \rightarrow {}^5G_6$ (377 nm). However, the relative intensities of these narrow absorption bands were very low in comparison to the strong broadband of the Ce^{3+} ion. This result indicated that the indirect excitation process of the Tb^{3+} ion *via* the 4f($^2F_{5/2}$) → 5d interconfigurational transition of the Ce^{3+} ion was more operative than under direct 4f^8–4f^8 transitions of the Tb^{3+} ion in the nanophosphors.

The emission spectra of the Fe_3O_4/ZnS@LaF_3:xCe^{3+},xGd^{3+},yTb^{3+} (x = 5; y = 5, 10 and 15 mol%) bifunctional nanomaterials were

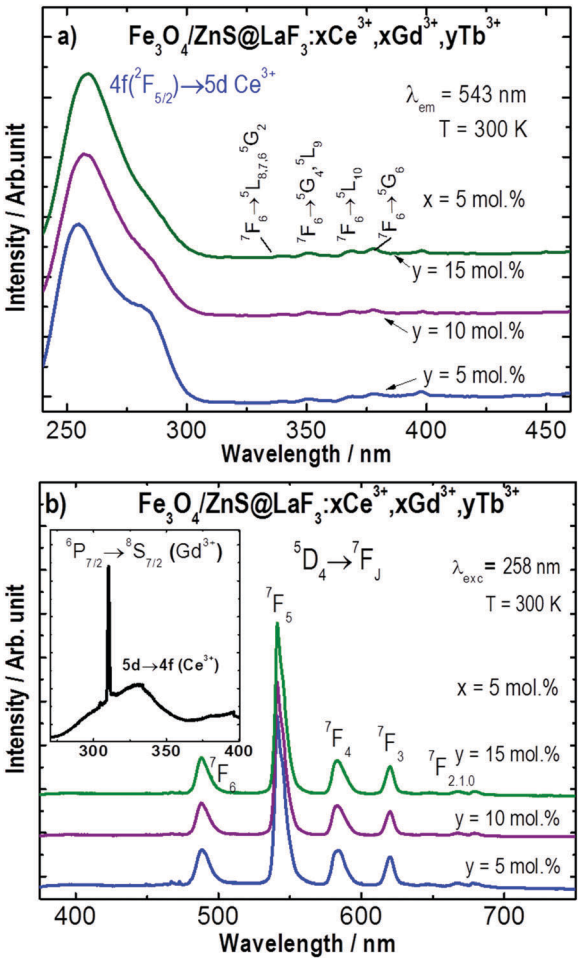

Fig. 6 Luminescence spectra of the Fe_3O_4/ZnS@LaF_3:$x$$Ce^{3+}$,$x$$Gd^{3+}$,$y$$Tb^{3+}$ nanophosphors, recorded at room temperature (300 K): (a) excitation spectra, monitoring emission at 543 nm assigned to the $^5D_4 \rightarrow {}^7F_5$ transition and (b) emission spectra upon excitation at 258 nm which corresponds to the $4f(^2F_{5/2}) \rightarrow 5d$ interconfigurational transition of the Ce^{3+} ion (inset figure shows the amplified spectral range of the Ce^{3+} and Gd^{3+} transitions).

recorded from 375 nm to 750 nm at 300 K (Fig. 6b) upon excitation at 258 nm, assigned to the $4f(^2F_{5/2}) \rightarrow 5d$ transition of the Ce^{3+} ion. The spectral range from 475 nm to 700 nm displayed narrow emission bands which have been assigned to the $^5D_4 \rightarrow {}^7F_J$ transitions (J = 6, 5, 4, 3, 2, 1 and 0) of the Tb^{3+} ion. Furthermore, the $^5D_4 \rightarrow {}^7F_5$ transition at 543 nm was the most intense and dominant for all the Fe_3O_4/ZnS@LaF_3:RE^{3+} nanophosphors. In addition, a very low intensity emission broadband was observed in the spectral range of 270 nm to 400 nm (inset, Fig. 6b). It was assigned to the $4f(^2F_{5/2}) \rightarrow 5d$ interconfigurational transition of the Ce^{3+} ion. However, a very narrow emission band at 310 nm in the same emission range was also assigned to the $^6P_{7/2} \rightarrow {}^8S_{7/2}$ transition of the Gd^{3+} ion.[46] This result indicated that the Ce^{3+} ion has been an efficient luminescent sensitizer to the Tb^{3+} ion (luminescent activator) for these nanophosphors (Fig. 7) through the energy transfer (ET) process. The luminescence spectra of the reference samples LaF_3:$x$$Ce^{3+}$,$x$$Gd^{3+}$,$y$$Tb^{3+}$ (x = 5; y = 5 and 10 mol%)

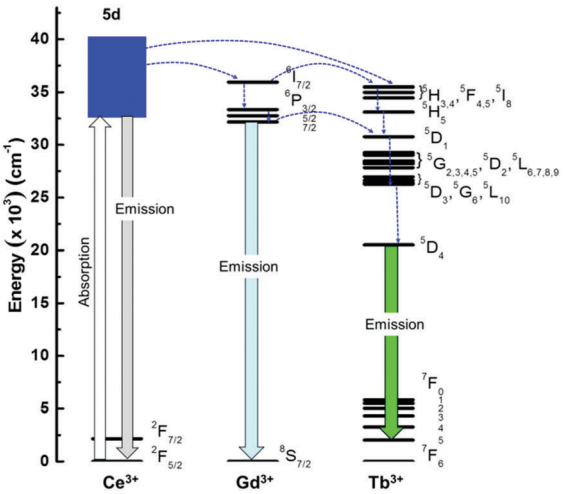

Fig. 7 Partial energy-level diagram of the Fe_3O_4/ZnS@LaF_3:$x$$Ce^{3+}$,$x$$Gd^{3+}$,$y$$Tb^{3+}$ nanophosphors presenting energy transfer (ET) processes from the sensitizer (Ce^{3+}) to the Gd^{3+} and Tb^{3+} activator ions. The dashed arrows represent nonradiative decays; and the gray, sky blue and green color downward arrows correspond to the radiative decay of the Ce^{3+}, Gd^{3+} and Tb^{3+} ions, respectively.

in the ESI† (Fig. S2) showed unaltered luminescence properties when compared to the bifunctional nanocomposites.

From the excitation/emission data, the nonradiative energy transfer (ET) pathways among the Ce^{3+}, Gd^{3+} and Tb^{3+} ions are described through the schematic energy level diagram for the Fe_3O_4/ZnS@LaF_3:$x$$Ce^{3+}$,$x$$Gd^{3+}$,$y$$Tb^{3+}$ nanophosphors (Fig. 7). A simplified energy transfer process for these bifunctional NPs can be described as follows: (i) a strong absorption from the $^2F_{5/2}$ ground state to the 5d excited state of the Ce^{3+} ion leading to a weak emission from 5d to $^2F_{5/2}$ states; (ii) a nonradiative energy transfer pathway from the 5d state of the cerium ion to the $^6I_{7/2}$ excited state of the Gd^{3+} ion that decays non-radiatively to the $^6P_{7/2}$ emitting level resulting in weak UV emission assigned to the $^6P_{7/2} \rightarrow {}^8S_{7/2}$ transition and (iii) a direct energy transfer from the 5d (Ce^{3+}) and $^6P_{7/2}$ (Gd^{3+}) states to the $4f^8$ intraconfigurational excited states of the Tb^{3+} ion. In this energy transfer process, the Gd^{3+} ion provides another energy transfer pathway between the sensitizer (Ce^{3+}) and activator (Tb^{3+}) ions.[47] However, the high intensity green emission line ($^5D_4 \rightarrow {}^7F_5$) is dominant in the emission spectra of all Fe_3O_4/ZnS@LaF_3:RE^{3+} nanophosphors. It is suggested that the Fe_3O_4/ZnS@LaF_3:RE^{3+} nanophosphors are promising materials for magnetic and green light-converting molecular devices (MLMCDs).

The lifetime values (τ) of the emitting $^5D_4$ level of the Tb^{3+} ion were determined from the luminescence decay curves of the bifunctional nanomaterials, which were measured at 300 K by monitoring emission at 543 nm of the $^5D_4 \rightarrow {}^7F_5$ transition of the Tb^{3+} ion and excitation at 258 nm. By fitting the curves with an exponential function of $I(t) = I_0 \exp(-t/\tau)$, mono-exponential decay behavior was observed. The normalized luminescence decay curves of the Fe_3O_4/ZnS@LaF_3:$x$$Ce^{3+}$,$x$$Gd^{3+}$,$y$$Tb^{3+}$ nanomaterials have been shown in Fig. 8. The lifetime τ values were found to be increased from 7.40 to 7.83 ms as the concentration of the dopant

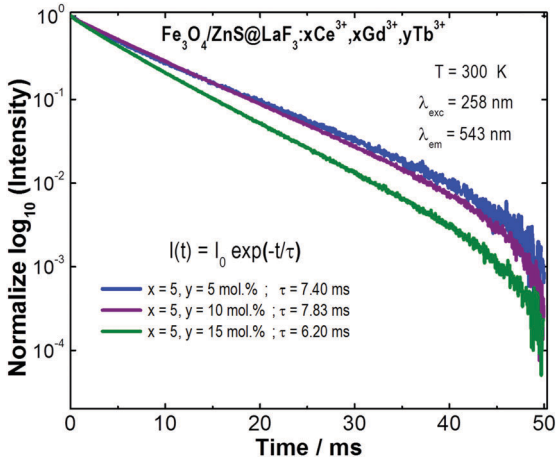

Fig. 8 Normalized luminescence decay curves of the Fe_3O_4/ZnS@LaF_3:$x$$Ce^{3+}$,$x$$Gd^{3+}$,$y$$Tb^{3+}$ (x = 5; y = 5, 10 and 15 mol%) nanophosphors, monitoring excitation at 358 nm corresponding to the 4f($^2F_{5/2}$) → 5d interconfigurational transition of the Ce^{3+} ion and emission at 543 nm, assigned to the $^5D_4$ → $^7F_5$ transition of the Tb^{3+} ion.

Tb^{3+} ion was increased from 5 to 10 mol%. However, this value decreased to 6.40 ms, as the concentration of the dopant Tb^{3+} ion was increased to 15 mol%, showing concentration quenching,[48] which might be due to the cross-relaxation process among the Tb^{3+} ions. This process depends on the interaction between two luminescent centers (Tb^{3+} ions) and quenches higher-level emissions by cross-relaxation. The cross-relaxation in Tb^{3+} ions may occur as follows:

$$Tb^{3+}\ (^5D_3) + Tb^{3+}\ (^7F_6) \rightarrow Tb^{3+}\ (^5D_4) + Tb^{3+}\ (^7F_0)$$

The emission color of green-emitting nanomaterials was evaluated by *Commission Internationale de l'éclairage* – CIE chromaticity diagram (Fig. 9). The overall emission color was calculated and expressed according to the (x, y) CIE color coordinates, which has been marked as A (0.367, 0.513), B (0.361, 0.535) and C (0.384, 0.513) for the x = 5; y = 5, 10 and 15 mol% samples, respectively. The green emission color was mainly due to the highest emission intensity contribution of the $^5D_4$ → $^7F_5$ transition of the Tb^{3+} ion (inset, Fig. 9).

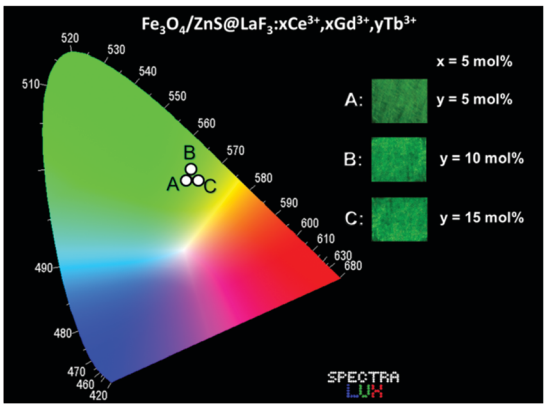

Fig. 9 The CIE chromaticity diagram of green-emitting magnetic Fe_3O_4/ZnS@LaF_3:$x$$Ce^{3+}$,$x$$Gd^{3+}$,$y$$Tb^{3+}$ (x = 5; y = 5, 10 and 15 mol%) nanophosphors. Photographs of nanomaterials (inset), taken using a digital camera, display green emission under UV irradiation at 254 nm.

3.3. Magnetic investigation

The magnetic properties using hysteresis loops (M–H curves) were measured using a SQUID magnetometer at 300 K and 5 K. At 300 K, the hysteresis loops (Fig. 10) of the Fe_3O_4, Fe_3O_4/ZnS and Fe_3O_4/ZnS@LaF_3:$x$$Ce^{3+}$,$x$$Gd^{3+}$,$y$$Tb^{3+}$ (x = 5; y = 5, 10 and 15 mol%) nanomaterials showed superparamagnetic (SPM) behavior with null or very low value of coercive field H_c (<25 Oe) and remanence (Fig. 10b).

The saturation magnetization (M_s) values were found to be 40.44 emu g^{-1} and 36.47 emu g^{-1} for Fe_3O_4 and Fe_3O_4/ZnS, respectively. The bifunctional Fe_3O_4/ZnS@LaF_3:$x$$Ce^{3+}$,$x$$Gd^{3+}$,$y$$Tb^{3+}$ nanomaterials showed M_s to be nearly 32.96 emu g^{-1} (x = 5; y = 5 mol%), 32.40 emu g^{-1} (x = 5; y = 10 mol%) and 34.41 emu g^{-1} (x = 5; y = 15 mol%) (Fig. 10a). This was attributed to the variance in particle size distribution, hence prolonged existence relaxation of nanostructures and noncollinear spin arrangement

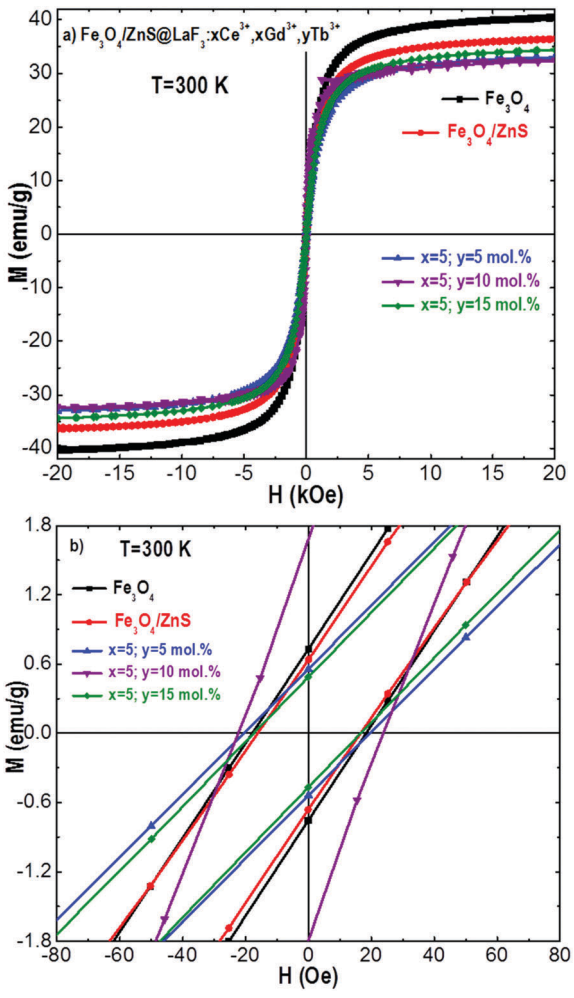

Fig. 10 Magnetization per gram of iron oxide as a function of magnetic field (M–H) of Fe_3O_4, Fe_3O_4/ZnS and Fe_3O_4/ZnS@LaF_3:$x$$Ce^{3+}$,$x$$Gd^{3+}$,$y$$Tb^{3+}$ (x = 5; y = 5, 10 and 15 mol%) nanomaterials, (a) at 300 K and (b) zoom-in view at 300 K showing coercive field magnitude.

in the nanoentities.[49,50] The reduced value of M_s revealed the functionalization of Fe_3O_4 with ZnS and further grafting by LaF_3:xCe^{3+},xGd^{3+},yTb^{3+}. Moreover, the decreased value of M_s of iron oxide from the bulk value (92 emu g^{-1}) was mainly due to coating of oleic acid over the Fe_3O_4 NPs during synthesis. The major contribution in magnetization was from the iron oxide nanoparticles. The mass fraction of the magnetic material attached is one of the factors that may affect the M_s to some extent.[51] The M_s of Fe_3O_4/ZnS was decreased due to the contribution of a low mass fraction of the ZnS with Fe_3O_4. The overall magnetic contribution for magnetic green-emitting nanomaterials was less than Fe_3O_4/ZnS by considering the mass contribution of magneto-luminescent materials for all x = 5; y = 5, 10 and 15 mol%. The M_s of the bifunctional nanocomposite varies from 32.40 emu g^{-1} to 34.41 emu g^{-1}, and it showed a very small increase in the M_s value when the Tb^{3+} ion concentration was increased (Fig. 10a). Although the M_s values of the luminescent and magnetic nanomaterials were lower when compared to that of the Fe_3O_4 core nanoparticles, they showed strong response to the external applied magnetic field.

Furthermore, the hysteresis curves (M–H) at 5 K and zero field cooling/field cooling (ZFC/FC) curves are displayed in Fig. S3 of ESI,† showing increased M_s values at 5 K and a very small magnetic contribution of RE^{3+} ions.

The combination of luminescence and magnetic characteristics showed appreciable luminescence intensity from the nanomaterial under an external magnetic field. It depicts the potential application of bifunctional nanomaterials for magnetic targeting and separation. This nanocomposite can show better performance by tuning simultaneously the magnetic and luminescence bifunctionality. The combination of magnetic and photoluminescence properties of the green-emitting magnetic nanocomposite is shown in Fig. 11, which displays a successful alliance of magneto-luminescence characteristics of the Fe_3O_4/ZnS@LaF_3:RE^{3+} nanomaterial.

In a cuvette, the material was dispersed in ethanol, displaying bright green emission under UV radiation. After placing the external bar magnet close to the cuvette, all particles of the sample moved quickly and stacked at a single place along one side of the cuvette in a clear solution of ethanol. This showed that the materials possessed strong magnetic characteristics.

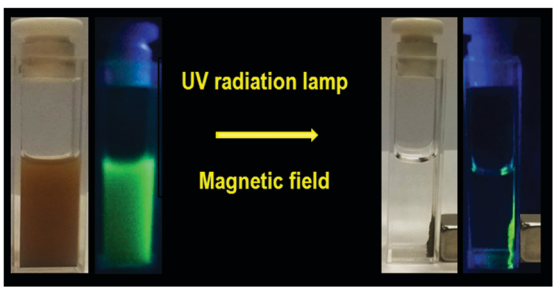

Fig. 11 digital photograph of the Fe_3O_4/ZnS@LaF_3: xCe^{3+},xGd^{3+},yTb^{3+} (x = 5; y = 15 mol%) nanocomposite dispersed in ethanol without (left) and with an external magnet (right) under UV irradiation at 254 nm.

Besides, upon exposure to ultraviolet radiation of 254 nm, bright green light was observed from the same corresponding place on the side wall of the cuvette near the magnet (Fig. 11, right). This complete procedure indicates that these bifunctional NPs possessed clear strong magnetic and luminescence properties in conjugation.

4 Conclusion

The luminescence and magnetic nanocomposites containing triply-doped Fe_3O_4/ZnS@LaF_3:xCe^{3+},xGd^{3+},yTb^{3+} (x = 5; y = 5, 10, 15 mol%) were successfully prepared by a multistep synthesis procedure. ZnS which was used as a spacer between the direct linkage of Fe_3O_4 and green LaF_3:RE^{3+} phosphors played its role well. This bifunctional nanomaterial displayed good emission intensity from the $^5D_4 \rightarrow {}^7F_{6-0}$ transitions of the Tb^{3+} ion when excited at the 4f $\rightarrow$ 5d interconfigurational transition of Ce^{3+} and supported by the Gd^{3+} ion. The luminescence decay curves suggested probable concentration quenching for the $^5D_4 \rightarrow {}^7F_5$ transition of the Tb^{3+} ion by cross-relaxation. Structural and morphological studies using X-ray diffraction and HR-TEM with EDS mappings in the scanning TEM mode, supported by DC magnetic properties, revealed the high magnetic saturation and the nanocrystalline superparamagnetic nature of the bifunctional nanocomposite at 300 K. As a result, this magneto-luminescent bifunctional nanocomposite may act as a good candidate for the preparation of emitting layers in magnetic and light-converting molecular devices (MLCMDs) and radiation detection or in down-shift applications through magnetic manipulation.

Acknowledgements

The authors are grateful for financial support from the Coordenação de Aperfeiçoamento de Pessoal de Nível Superior (CAPES, Brazil), the Fundação de Amparo à Pesquisa do Estado de Maranhão (FAPEMA, Brazil), the Conselho Nacional de Desenvolvimento Científico e Tecnológico (CNPq, Brazil), the Fundação de Amparo à Pesquisa do Estado de São Paulo (FAPESP, Brazil), the Consejo Nacional de Investigaciones Científicas y Técnicas (CONICET, Argentina), the Centro Nacional de Pesquisa em Energia e Materiais (CNPEM-LNNano, Brazil), and Jan Ringnalda (Thermo Fisher Scientific, FEI Company) for the HAADF and EDS mapping images acquired during the operational training of the Titan Themis microscope, recently installed in Laboratório Nacional de Nanotecnologia (LNNano).

References

1 L. U. Khan, D. Muraca, H. F. Brito, O. Moscoso-Londoño, M. C. F. C. Felinto, K. R. Pirota, E. E. S. Teotonio and O. L. Malta, *J. Alloys Compd.*, 2016, **686**, 453–466.
2 L. U. Khan, H. F. Brito, J. Hölsä, K. R. Pirota, D. Muraca, M. C. F. C. Felinto, E. E. S. Teotonio and O. L. Malta, *Inorg. Chem.*, 2014, **53**, 12902–12910.

3 G. Konstantatos and E. H. Sargent, *Nat. Nanotechnol.*, 2010, **5**, 391–400.
4 C. Lorbeer and A. V. Mudring, *J. Phys. Chem. C*, 2013, **117**, 12229–12238.
5 O. Chen, L. Riedemann, F. Etoc, H. Herrmann, M. Coppey, M. Barch, C. T. Farrar, J. Zhao, O. T. Bruns, H. Wei, P. Guo, J. Cui, R. Jensen, Y. Chen, D. K. Harris, J. M. Cordero, Z. Wang, A. Jasanoff, D. Fukumura, R. Reimer, M. Dahan, R. K. Jain and M. G. Bawendi, *Nat. Commun.*, 2014, **5**, 5093.
6 J. B. Haun, T. J. Yoon, H. Lee and R. Weissleder, *Wiley Interdiscip. Rev.: Nanomed. Nanobiotechnol.*, 2010, **2**, 291–304.
7 F. Ye, Å. Barrefelt, H. Asem, M. Abedi-Valugerdi, I. El-Serafi, M. Saghafian, K. Abu-Salah, S. Alrokayan, M. Muhammed and M. Hassan, *Biomaterials*, 2014, **35**, 3885–3894.
8 A. Son, A. Dhirapong, D. K. Dosev, I. M. Kennedy, R. H. Weiss and K. R. Hristova, *Anal. Bioanal. Chem.*, 2008, **390**, 1829–1835.
9 O. S. Wolfbeis, *Chem. Soc. Rev.*, 2015, **44**, 4743–4768.
10 A. Espinosa, R. D Corato, J. Kolosnjaj-Tabi, P. Flaud, T. Pellegrino and C. Wilhelm, *ACS Nano*, 2016, **10**, 2436–2446.
11 D. Shi, M. E. Sadat, A. W. Dunn and D. B. Mast, *Nanoscale*, 2015, **7**, 8209–8232.
12 F. Zhang, G. B. Braun, A. Pallaoro, Y. Zhang, Y. Shi, D. Cui, M. Moskovits, D. Zhao and G. D. Stucky, *Nano Lett.*, 2012, **12**, 61–67.
13 S. Gai, P. Yang, C. Li, W. Wang, Y. Dai, N. Niu and J. Lin, *Adv. Funct. Mater.*, 2010, **20**, 1166–1172.
14 H. Kim, M. Achermann, L. P. Balet, J. A. Hollingsworth and V. I. Klimov, *J. Am. Chem. Soc.*, 2005, **127**, 544–546.
15 C. Kaewsaneha, P. Tangboriboonrat, D. Polpanich and A. Elaissari, *ACS Appl. Mater. Interfaces*, 2015, **7**, 23373–23386.
16 Y.-S. Lin, S. Wu, Y. Hung, Y. Chou, C. Chang, M. Lin, C. Tsai and C.-Y. Mou, *Chem. Mater.*, 2006, **18**, 5170–5172.
17 L. Zhang, B. Liu and S. Dong, *J. Phys. Chem. B*, 2007, **111**, 10448–10452.
18 X. Hong, J. Li, M. Wang, J. Xu, W. Guo, J. Li, Y. Bai and T. Li, *Chem. Mater.*, 2004, **16**, 4022–4027.
19 W. Wu, Q. He and C. Jiang, *Nanoscale Res. Lett.*, 2008, **3**, 397–415.
20 C.-J. Yu, S.-M. Wu and W.-L. Tseng, *Anal. Chem.*, 2013, **85**, 8559–8565.
21 A. Roychowdhury, S. P. Pati, S. Kumar and D. Das, *AIP Conf. Proc.*, 2013, **1512**, 246–247.
22 L. Liu, W. Jiang, L. Yao, X.-W. Yang, B.-H. Chen, S.-X. Wu and F.-S. Li, *J. Nanosci. Nanotechnol.*, 2014, **14**, 5047–5053.
23 C. Zhang, B. Pu, Z. Mo and C. Jiang, *Micro Nano Lett.*, 2014, **9**, 171–174.
24 M. Stefan, C. Leostean, O. Pana, M. L. Soran, R. C. Suciu, E. Gautron and O. Chauvet, *Appl. Surf. Sci.*, 2014, **288**, 180–192.
25 K. Binnemans, *Chem. Rev.*, 2009, **109**, 4283–4374.
26 A. S. Borges, J. D. L. Dutra, R. O. Freire, R. T. Moura, J. G. Da Silva, O. L. Malta, M. H. Araujo and H. F. Brito, *Inorg. Chem.*, 2012, **51**, 12867–12878.
27 J.-C. G. Bünzli, *Coord. Chem. Rev.*, 2015, **293–294**, 19–47.
28 W. T. Carnall, G. L. Goodman, K. Rajnak and R. S. Rana, *J. Chem. Phys.*, 1989, **90**, 3443–3457.
29 *Spectroscopic Properties of Rare Earths in Optical Materials*, ed. G. Liu and B. Jacquier, Springer-Verlag Berlin, Heidelberg, 2005, ch. 1, pp. 1–94.
30 H. F. Brito, O. L. Malta, M. C. F. C. Felinto and E. E. S. Teotonio, in *Lumin. Phenom. Involv. Met. Enolates. Chem. Met. Enolates.*, ed. J. Zabicky, John Wiley Sons Ltd, England, 2009, pp. 131–184.
31 J. M. D. Coey, *Magnetism and magnetic materials*, Cambridge University Press, Cambridge, 2010.
32 X. Sun, Y. W. Zhang, Y. P. Du, Z. G. Yan, R. Si, L. P. You and C. H. Yan, *Chem. – Eur. J.*, 2007, **13**, 2320–2332.
33 A. R. Denton and N. W. Ashcroft, *Phys. Rev. A: At., Mol., Opt. Phys.*, 1991, **43**, 3161–3164.
34 J.-C. G. Bunzli and C. Piguet, *Chem. Soc. Rev.*, 2005, **34**, 1048–1077.
35 S.-Y. Yu, H.-J. Zhang, J.-B. Yu, C. Wang, L.-N. Sun and W.-D. Shi, *Langmuir*, 2007, **23**, 7836–7840.
36 F. N. Sayed, V. Grover, S. V. Godbole and A. K. Tyagi, *RSC Adv.*, 2012, **2**, 1161–1167.
37 E. Sarantopoulou, S. Kobe, Z. Kollia, P. J. McGuiness and A.-C. Cefalas, *IEEE Trans. Magn.*, 2003, **39**, 3426–3428.
38 J. M. Vargas, J. J. Blostein, I. Sidelnik, D. R. Brito and L. A. R. Palominoa, *J. Instrum.*, 2016, DOI: 10.1088/1748-0221/11/09/P09007.
39 Y. Liu, W. Chen, S. Wang, A. G. Joly, S. Westcott and B. K. Woo, *J. Appl. Phys.*, 2008, **103**, 063105.
40 M. Osinski, *et al.*, Thermal neutron detectors based on gadolinium-containing nanoscintillators, United States, Patent Application Publication (13/506,240), Pub. No.: US 2010/0041620 A1 Publication Classi – 250/390.11; 250, 2012.
41 X. Wang, J. Zhuang, Q. Peng and Y. Li, *Nature*, 2005, **437**, 121–124.
42 X. Yu, J. Wan, Y. Shan, K. Chen and X. Han, *Chem. Mater.*, 2009, **21**, 4892–4898.
43 K. Sankar, J. B. Plumley, B. A. Akins, T. A. Memon, N. J. Withers, G. A. Smolyakov and M. Osinski, *Proc. of SPIE*, 2009, **7189**, 718909.
44 B. Poornaprakash, D. Amaranatha Reddy, G. Murali, N. Madhusudhana Rao, R. P. Vijayalakshmi and B. K. Reddy, *J. Alloys Compd.*, 2013, **577**, 79–85.
45 Y. Jiang, X. M. Meng, J. Liu, Z. Y. Xie, C. S. Lee and S. T. Lee, *Adv. Mater.*, 2003, **15**, 323–327.
46 H. He, M. Y. Xie, Y. Ding and X. F. Yu, *Appl. Surf. Sci.*, 2009, **255**, 4623–4626.
47 L. Liu, N. Zhang, Z. Leng, Y. Liang, R. Li, L. Zou and S. Gan, *Dalton Trans.*, 2015, **44**, 6645–6654.
48 J. Lian, X. Sun and X. Li, *Mater. Chem. Phys.*, 2011, **125**, 479–484.
49 Q. A. Pankhurst and R. J. Pollard, *Phys. Rev. Lett.*, 1991, **67**, 248–250.
50 P. M. A. de Bakker, E. De Grave, R. E. Vandenberg and L. H. Bowen, R. J. Pollard and P. R.M., *Phys. Chem. Miner.*, 1991, **18**, 131–143.
51 B. Poornaprakash, K. Naveen Kumar, U. Chalapathi, M. Reddeppa, P. T. Poojitha and S.-H. Park, *J. Mater. Sci.: Mater. Electron.*, 2016, **27**, 6474–6479.

